Received 21 December 2022; revised 17 February 2023; accepted 25 February 2023. Date of publication 8 March 2023; date of current version 21 March 2023.

Digital Object Identifier 10.1109/OJAP.2023.3253942

Highly Efficient Calibration of Antenna Arrays by Active Targets in the Near-Field

MATTHIAS LINDER (Graduate Student Member, IEEE), BENEDIKT MEINECKE (Member, IEEE), ENES HALICI, DOMINIK SCHWARZ (Graduate Student Member, IEEE), AND CHRISTIAN WALDSCHMIDT (Fellow, IEEE)

Institute of Microwave Engineering, Ulm University, 89081 Ulm, Germany

CORRESPONDING AUTHOR: M. LINDER (e-mail: matthias.linder@uni-ulm.de)

ABSTRACT To enhance the capabilities of high-resolution imaging or beamforming, the trend goes towards arrays with high-channel count and large aperture sizes. The operation at increasing mm-wave frequencies exacerbates the consequences of manufacturing tolerances on the array performance, further necessitating the development of high-quality calibrations. Thereby, a large number of array response vectors, addressed in the following as data points, is stored. Typically, one data point is measured at a time for each angle. To reduce the calibration effort, hereby defined as the number of required measurements, a calibration setup employing active calibration targets (ACT) is proposed. This setup allows the storage of a multitude of data points within a single measurement. In addition, this measurement setup is placed in the near-field of the array to relax the requirements on the size of the anechoic chamber. Employing multiple targets makes it challenging to compensate the near-field effects. Therefore, methods are discussed to ensure a consistent quality of the calibration considering the near-field influences from the ACTs. Exemplary measurements deploying an antenna array operating at 78.5 GHz demonstrate that this calibration measurement setup employing three ACTs placed in the near-field of the array reduces the calibration effort by a factor of 3 compared to state-of-the-art setups. The average deviation of the antenna phase relations amounts to 4.1 degree, proving that the presented setup achieves the same calibration quality as state-of-the-art setups.

INDEX TERMS Calibration, direction-of-arrival (DoA) estimation, imaging radar, MIMO radar, phased arrays, radar measurements.

I. INTRODUCTION

PHASED arrays and millimeter-wave imaging radars have many applications in civil and military domains [1], [2], [3], [4], [5], [6]. These systems are employed for measurements of the direction-of-arrival (DoA) estimation of incoming waves or beamforming at the transmitter. Latest works focus on the DoA estimation in azimuth and elevation to achieve 4D imaging [7], [8], [9]. As these operations require a precise array model, calibration of the antenna array is crucial. Effects like manufacturing tolerances, varying feed line lengths, and mutual antenna coupling lead to deviations of the ideal array response. These effects become even more significant in the upper mm-wave frequency range [10]. Therefore, a measurement of the array response vector has to be performed [11], [12], [13] to adjust the array model. This adjustment can be performed either by means of calibration parameters, namely the antenna positions (antenna phase centers) and phase offsets [10] or alternatively non-parametrically applying a calibration matrix, which contains the obtained angle-dependent reference measurements [14]. Thus, systematic errors during the subsequently performed DoA estimation can be avoided [15].

Particularly for large-aperture sizes, the calibration effort increases drastically [14]. Therefore, enhancements in calibration techniques are needed to obtain accurate antenna array models with low measurement effort during the calibration procedure [16], [17]. A typical calibration setup is sketched in Fig. 1. The array under test (AuT) is mounted on

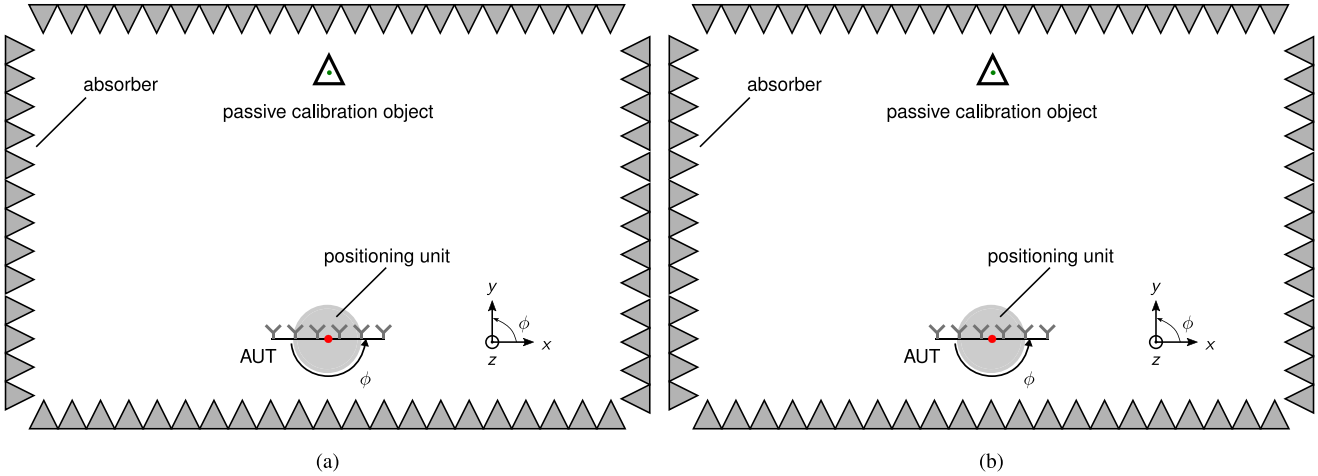

FIGURE 1. Angular array calibration setup in an anechoic chamber: The stationary calibration object is ideally located in the far-field of the antenna array. The array is rotated by the positioning system, which translates into a movement of the calibration object on a spherical trajectory. Depicted are a conventional calibration setup (a) and the desired final calibration setup proposed in this work (b).

a rotatable positioning system. At each angular step, a measurement with a stationary calibration target is performed, and the array response vector for this data point is captured. Common calibration targets are corner reflectors, as they ensure a high SNR. Typically, a single calibration target is used. For a total of N_i data points, the same amount of rotation steps is needed. For large-aperture arrays, this leads to a significant duration of the calibration measurement.

Highly efficient calibration methods have been developed that require a low number of data points [17], [18] but at the cost of a high computational effort. To decrease the calibration effort, the recording of a multitude of data points within a single measurement snapshot by applying active calibration targets (ACT) placed at different angles is proposed. This procedure can also be combined with efficient calibration methods like [17]. When applying N_T ACTs, the calibration effort can be reduced by a factor of N_T, as N_T data points are recorded within a single snapshot. In this article, an advanced calibration setup with $N_\mathrm{T} = 3$ as in Fig. 1(b) is aimed for. To further relax requirements on the anechoic chamber, the calibration measurement is performed in the near-field region of the AUT, leading to the dashed anechoic chamber size. The positioning of ACTs in the near-field region, where a plane wave can no longer be assumed, leads to effects that must be compensated for [19]. Common calibration techniques in the near-field of the AuT consider one passive target [19], [20]. The compensation of multiple active targets increase the complexity and necessitate new methods.

This article is organized as follows: In Section II, the calibration using an ACT is described mathematically and investigated by simulations and measurements. The fusion of data sets recorded with several ACTs is conducted in Section III, the derived theory is proven by measurements and a procedure for efficient calibration of the measurement setup is described. In Section IV, the calibration measurement is performed with an ultra-compact setup using three ACTs. For the compensation of near-fields effects by a path model, the determination of the required parameters from calibration measurements is described. Further, the influence of target alignment inaccuracies is investigated. Finally, the near-field effects are compensated, and the calibration parameters are compared to the calibration parameters obtained from a reference setup with a single corner reflector positioned in the far-field of the AUT.

II. ARRAY CALIBRATION WITH AN ACTIVE CALIBRATION TARGET

The calibration setup employing ACTs requires adjustments of the calibration procedure. These adjustments are explained in this section. First of all, the general array calibration and DOA estimation is explained. Afterwards, the target detection for ACTs is described, followed by investigations of the bistatic target influence and the compensation of it.

A. GENERAL ARRAY CALIBRATION AND DOA ESTIMATION

For the calibration procedure, the array response vector $a(\phi)$ is measured versus the desired DoA range [14]. For an incident plane wave impinging at an azimuth angle ϕ, the array response vector is [11]

$$a_i(\phi) = \begin{pmatrix} A_1(\phi)\mathrm{e}^{\mathrm{j}\left(\frac{2\pi}{\lambda_0}x_1\sin(\phi)+\psi_1\right)} \\ \vdots \\ A_{N_\mathrm{RX}}(\phi)\mathrm{e}^{\mathrm{j}\left(\frac{2\pi}{\lambda_0}x_{N_\mathrm{RX}}\sin(\phi)+\psi_{N_\mathrm{RX}}\right)} \end{pmatrix} \tag{1}$$

with $i \in [1, I]$, where I is the total number of angular sampling points, $A_k(\phi)$ the angle-dependent amplitude information for each receive antenna of index k, and N_RX the total number of RX antennas. The calibration parameters consist of the antenna position x_k and ψ_h as phase offset. Usually, the amplitude terms can be neglected if antennas with a wide beamwidth are used. Since this condition is met

in the majority of imaging systems, the amplitude term is omitted in this article.

A straightforward way to perform the DoA estimation is the deterministic maximum likelihood approach [21], where the measured array response vector at the virtual receive antennas (VX) is compared with a reference calibration matrix C. For multiple-input multiple-output (MIMO) radars, the measured signal phase corresponds to the sum of the phases at the TX and RX antennas. Usually, the definition of an equivalent VX antenna is used to describe this behaviour. The array response vector of the virtual array is thereby calculated as the Kronecker product of the transmit and the receive array response vectors [22]. Thus, the calibration matrix has the dimensions $I \times N_{\mathrm{VX}}$ and stores the array response vectors of all reference samples at different angles in the azimuth plane. The comparison between the received array response vector a and C is mathematically calculated as the cross-correlation

$$b(\phi) = \frac{\left|C^{\mathrm{H}}(\phi) \cdot a\right|}{\left|\left|C(\phi)\right|\right| \left|\left|a\right|\right|}, \tag{2}$$

with the symbol $(\cdot)^{\mathrm{H}}$ denoting the complex conjugate (Hermitian) matrix and $||\cdot||$ denoting the Euclidean norm. The DoA of the measured array response vector ϕ_{est} is determined by finding the direction that maximizes the cross-correlation

$$\phi_{\mathrm{est}} = \arg\max_{\phi} b(\phi). \tag{3}$$

Instead of measuring the complete calibration matrix, it can be modelled using the calibration parameters. This modelling is based on (1) and is restricted to scenarios with sufficiently large SNR. The calibration parameters can be obtained by the standard method as described, e.g., in [14]. Hereby, the antenna positions are determined from the slope of the phase progression versus the measured angle. The second calibration parameter is the phase offset, which is the phase relation of one antenna to the reference antenna while facing a target at boresight ($\phi = 0\,^{\circ}$) direction. The phase offsets are obtained after linearisation to achieve a higher robustness against noise. All calibration methods have in common that they require a specific amount of measurement points to ensure a certain quality of the determined calibration parameters [14], [17], [23], [24].

B. CALIBRATION CONCEPT WITH AN ACTIVE CALIBRATION TARGET

Calibration with several targets in parallel is only possible if these targets can be separated. Depending on the system, the targets can be separated by different methods. In case of an array employed for communication purposes, the separation takes place in the frequency-domain. A small frequency offset is added by modulating the received signal at the ACT. Thereby, small modulation frequencies are deployed to ensure approximately equal antenna characteristics. For radar operations, the separation can be conducted in the r-v-(range, velocity) domain. In the following, an FMCW radar is used as exemplary demonstrator. In case of passive calibration targets, these targets need to be placed in different range cells. This placement leads to several effects such as different near-field effects and range-angle coupling that have to be compensated for [19]. With the usage of ACTs, this requirement may be overcome. ACTs are used widely in radar target simulators [25], [26] to evaluate radar systems and to simulate not only different distances but also different velocities of targets [27]. Unlike passive targets, this allows target detection for ACTs through preset velocities. This possibility of target separation is used to build up an innovative measurement setup for calibrations using a variety of calibration targets in the same range of the AUT. The separation of the targets takes thus place in the v-domain. The operation principle of an ACT is depicted in Fig. 2. The RX antenna receives the incoming signal that is amplified by a variable gain amplifier (VGA). In order to implement the desired shift in v, the signal is modulated [28]. This modulation is deployed by a mixing operation performed by an IQ-mixer with the modulation frequency f_{mod}. A second VGA is employed to compensate for conversion losses of the mixer and to amplify the TX signal, which is then radiated by the TX antenna.

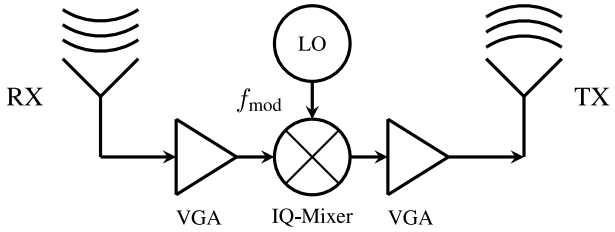

FIGURE 2. Block diagram of the ACT consisting of an RX- and a TX-antenna, two VGAs, an IQ-mixer, and an external local oscillator.

With the choice of the antenna types and the amplification of the signal by the VGA, the ACT provides more degrees of freedom as the corner reflector, which can only be adjusted with respect to its RCS value when scaled.

While the corner reflector acts as a point target, the ACTs have separated points of interaction for receive and transmit operation. Thus, the ACT represents a bistatic target and requires additional compensation depending on the measurement setup. Furthermore, when using ACTs, a free choice of r-v bins is made possible by signal modulation.

C. TARGET DETECTION FOR ACTIVE CALIBRATION TARGETS

At first, the corner reflector as commonly used calibration target is investigated. For the corner reflector, the point target assumption can be met representing a single target. The phase of the receive signal after down conversion is [29]

$$\begin{aligned}\Delta\psi(t) &= \psi(t) - \psi(t-\tau) \\ &= 2\pi\left(f_{\mathrm{c}}\tau + \frac{B}{T}t\tau - \frac{B}{2T}\tau^2\right)\end{aligned} \tag{4}$$

with the center frequency f_c, the bandwidth B of the signal, the ramp duration T, and the path delay $\tau = 2R/c_0$ resulting from the target distance R and the speed of light c_0. In reality, phase noise influences are present, which are neglected here. Eq. (4) shows that a separation of targets is only possible if they are located in different range cells. The separation of ACT targets at radar operation is not limited to FMCW operations, as shown here [30] for orthogonal frequency-division multiplexing (OFDM) operation.

Assuming that the path length for the wave propagating from the AUT's TX to the ACT's RX antenna $R_{\mathrm{TX,RX}}$ equals the path length from the ACT's TX antenna to the array's RX antenna $R_{\mathrm{RX,TX}}$ and neglecting the time duration caused by line lengths inside the ACT, the target phase at the receiver for the stationary ACT leads to a shift in range of [28]

$$\Delta R_{\mathrm{mod}} = \frac{f_{\mathrm{mod}} T_c c_0}{2B} \tag{5}$$

and a velocity shift of

$$\Delta v = \frac{f_{D,s} c_0}{2 f_c} \quad \text{with the velocity shift} \tag{6}$$

$$f_{D,s} = \begin{cases} \mathrm{mod}\left(f_{\mathrm{mod}}, \frac{1}{2T_{\mathrm{r}}}\right) \text{ if } \mathrm{mod}\left(\left\lfloor \frac{f_{\mathrm{mod}}}{\frac{1}{2T_{\mathrm{r}}}} \right\rfloor\right) = 0 \\ \mathrm{mod}\left(f_{\mathrm{mod}}, \frac{1}{2T_{\mathrm{r}}}\right) - \frac{1}{2T_{\mathrm{r}}} \quad \text{else} \end{cases} \tag{7}$$

with T_{r} as chirp repetition interval and f_{mod} as modulation frequency, introduced by the ACT's IQ-mixer. Even if positioned at the same distance to the antenna array, by supplying different modulation frequencies for the ACTs, they can be separated due to different measured velocities. Moreover, an undesired range shift is caused by the modulation frequency, that has to be compensated during the calibration procedure as this range shift falsifies the range measured. Since this range shift can be accurately predicted, it can be compensated with ease. In the simulation model, a wrong target distance can alter the near-field effects. In theory, this range shift can be used to separate the targets, in practice, this is more prone to errors as there are more distortions in the r- than in the v-domain. This can lead to a lower SNR of the receive signal or even that a wrong target is evaluated.

D. INFLUENCE OF THE BISTATIC TARGET

As the ACT possesses separated antennas for receiving and transceiving, the assumption of a point target in (4) is not valid anymore. If not compensated, this assumption can lead to systematic errors in the calibration procedure.

1) MATHEMATICAL MODEL

The geometry of the measurement setup for the simulation based on optical paths is depicted in Fig. 3. The signal emitted from the transceiver is received by the ACT, which in turn transmits it back to the AUT. At the u-th RX antenna of the AUT, the phase is defined as

$$\varphi_u(\phi) = -\mathrm{j}kd_{\mathrm{TX}}(\phi) + \varphi_{\mathrm{Target}} + \left(-\mathrm{j}kd_{\mathrm{RX},u}(\phi)\right) + \varphi_u, \tag{8}$$

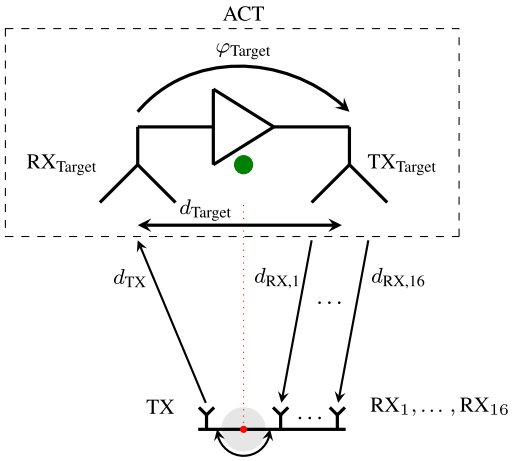

FIGURE 3. Sketch of the geometric model for the calibration measurement setup with active target consisting of an RX-, TX-antenna and, an amplifier. Dot ● marks the position of the corner reflector.

with the wave number k, the phase offset added by the ACT $\varphi_{\mathrm{Target}}$, the phase offsets of the u-th virtual antenna φ_{u}, and the path lengths from the AUT's TX to the ACT and ACT to the AUT's RX antenna $d_{\mathrm{TX/RX}}$. As the calibration method is only based on phase relations, the phase change ϕ_{Target} introduced by propagation through the ACT does not affect the relative phase at the u-th receive antenna referred to the w-th receive antenna:

$$\begin{aligned} \Delta\varphi_u(\phi) &= \varphi_u(\phi) - \varphi_w(\phi) \\ &= -\mathrm{j}kd_{\mathrm{TX}}(\phi) + \varphi_{\mathrm{Target}} + \left(-\mathrm{j}kd_{\mathrm{RX},u}(\phi)\right) + \varphi_u \\ &\quad - \left(-\mathrm{j}kd_{\mathrm{TX}}(\phi) + \varphi_{\mathrm{Target}} + \left(-\mathrm{j}kd_{\mathrm{RX},w}(\phi)\right) + \varphi_w\right) \\ &= -\mathrm{j}kd_{\mathrm{RX},u}(\phi) + \varphi_u - \left(-\mathrm{j}kd_{\mathrm{RX},w}(\phi)\right) - \varphi_w. \end{aligned} \tag{9}$$

In the following, all channels are referred to channel 1, which is closest to the rotation centre of the positioning system. Since some systematic errors exert almost the same influences on all channels, such as the inaccuracy of the positioning unit, these influences are reduced by referencing.

2) HARDWARE DEMONSTRATOR

To analyse this effect, a uniform linear array (ULA) is operated in a single-input multiple-output (SIMO) mode. A photograph of the antenna array is shown in Fig. 4(a). The antenna positions of the physical and virtual array are sketched in Fig. 4(b). As only the bistatic influence of an active target is investigated here, the mixer is not accounted for.

For analysis, the setup in Fig. 4(c) is employed, which consists of two horn antennas, a waveguide amplifier with a gain of 17.5 dB, and waveguide transmission lines as connectors. By adding waveguide transmission lines, the size of the target d_{Target}, associated with the distance between RX and TX antenna phase center, can be adjusted. The radar parameters applied with the SIMO operation are listed in Tab. 1.

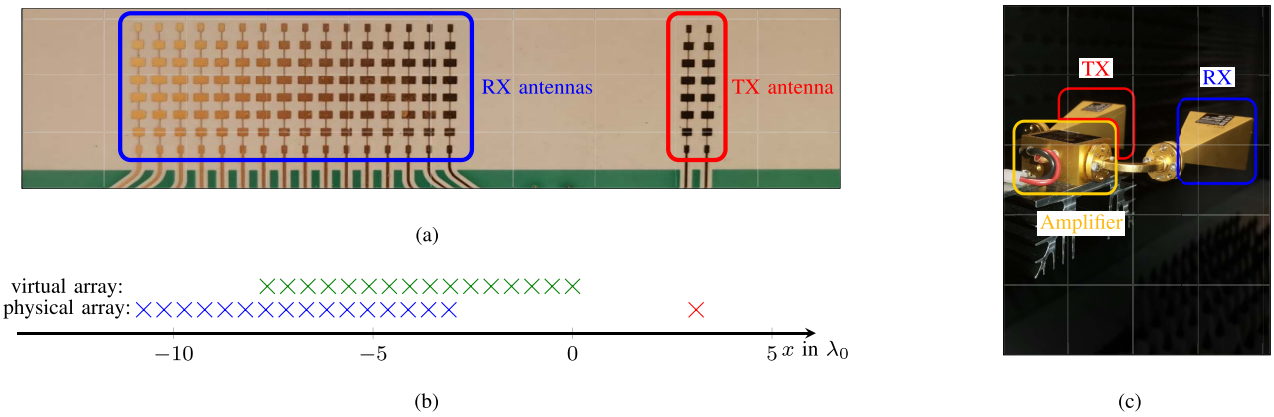

FIGURE 4. (a) Photograph of the realized radar frontend with 16 RX antennas and 1 TX antenna used. (b) Sketch of the positions of the TX antennas (×), RX antennas (×), and VX antennas (×). (c) Photograph of the hardware demonstrator.

TABLE 1. Overview of the SIMO operation radar parameters.

Ramp duration T	200 µs
Ramp repetition time T_r	220 µs
Center frequency f_c	77 GHz
RF bandwidth B	2 GHz
Number of chirps N_c	512
Number of virtual channels $N_{VX} = N_{TX} \cdot N_{RX}$	$16 = 1 \cdot 16$
Virtual aperture size A_V	$7.7\,\lambda_0$

3) VERIFICATION BASED ON MEASUREMENTS

To verify the mathematical model developed in the previous paragraph, three different measurement setups are deployed. As a reference, a calibration measurement with a conventional corner reflector with $\sigma = 14.4$ dBsm is conducted at a target distance of 4.7 m, which fulfills the far-field condition of the array. For analyzing the bistatic effects on the calibration procedure, the active target shown in Fig. 4(c) with two different antenna distances d_{Target}, namely 92 mm and 192 mm, is analyzed. Fig. 5 depicts the simulated and measured target phase referenced to the result of the corner reflector.

The simulations show that due to the bistatic target, phase errors occur depending on d_{Target}. A d_{Target} of 92 mm leads to a maximum error of 19.9°, while for a d_{Target} of 92 mm, a maximum error of 47.5° can be observed. In the measurement, the maximum errors are slightly lower with 17.1° and 46.6°, respectively. An average deviation of 1.1° for $d_{\text{Target}} = 92$ mm and 1.0° for $d_{\text{Target}} = 192$ mm verifies the correctness of the simulation model. Therefore, the influence of the separated TX and RX antennas of the active target can be compensated independently of the sizes if the setup's geometry is well known.

4) ACCURACY OF DETERMINED CALIBRATION PARAMETERS

To evaluate the quality of the calibration based on ACTs, the calibration parameters x_i and φ_i according to (1) are

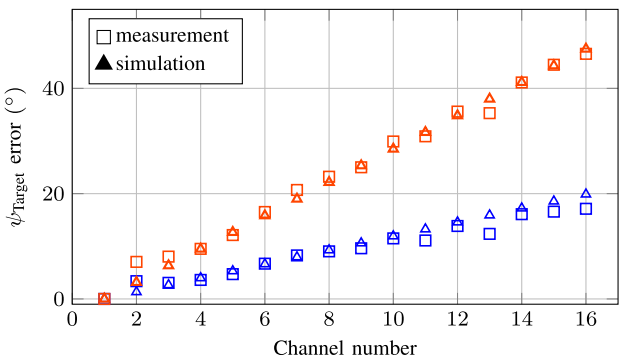

FIGURE 5. Measured and simulated results for the phase offsets for $d_{\text{Target}} = 92$ mm (–) and 192 mm (–) with the phase offsets determined from a measurement or simulation with a corner reflector as reference.

analyzed. The deviation of these parameters compared with those obtained from a conventional calibration measurement with a corner reflector as passive target are depicted in Fig. 6. The phase offsets in Fig. 6(a) are determined after compensating the bistatic influence of the target by means of the simulation model (9). The mean deviation is 1.1° for $d_{\text{Target}} = 92$ mm and 1.0° for $d_{\text{Target}} = 192$ mm. In Fig. 6(b), the deviations of the VX-antenna positions are plotted, where the mean deviation is $0.012\,\lambda_0$ for $d_{\text{Target}} = 92$ mm and $0.014\,\lambda_0$ for $d_{\text{Target}} = 192$ mm. As the calibration parameters obtained by bistatic targets agree well with the results of the conventional calibration, the feasibility of ACTs in calibration measurements is demonstrated.

III. DATA FUSION OF ACTIVE CALIBRATION TARGETS

In this section, the fusion of multiple data sets, obtained by different ACTs simultaneously, is derived and evaluated. This reduces the calibration effort, as a smaller number of measurements has to be conducted. First, the separability of targets by shifts in the velocity-domain is demonstrated by measurement. Afterwards, a calibration of the measurement setup is described. Finally, the fusion of data sets, recorded with multiple ACTs simultaneously, is conducted.

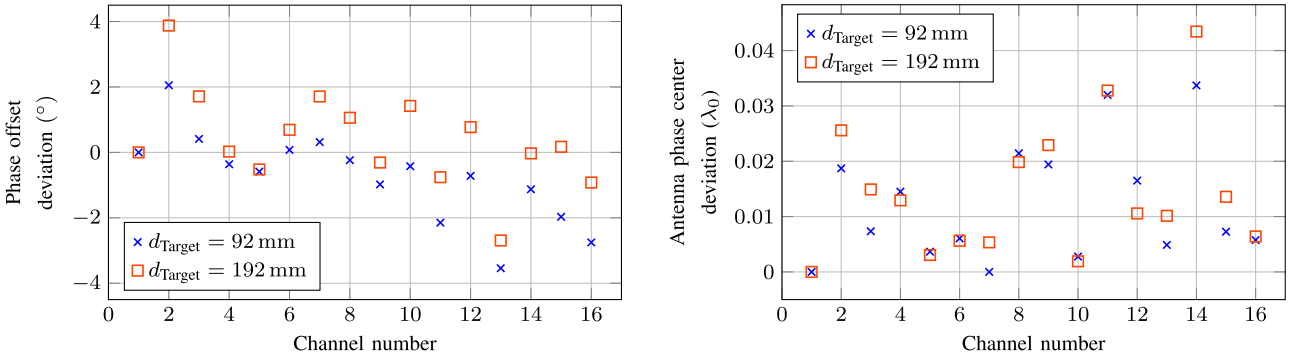

FIGURE 6. Deviation of the calibration parameters obtained with ACT referenced to calibration parameters obtained from measurement with a corner reflector. (a) Deviation of obtained phase offsets and (b) of VX-antenna phase centers.

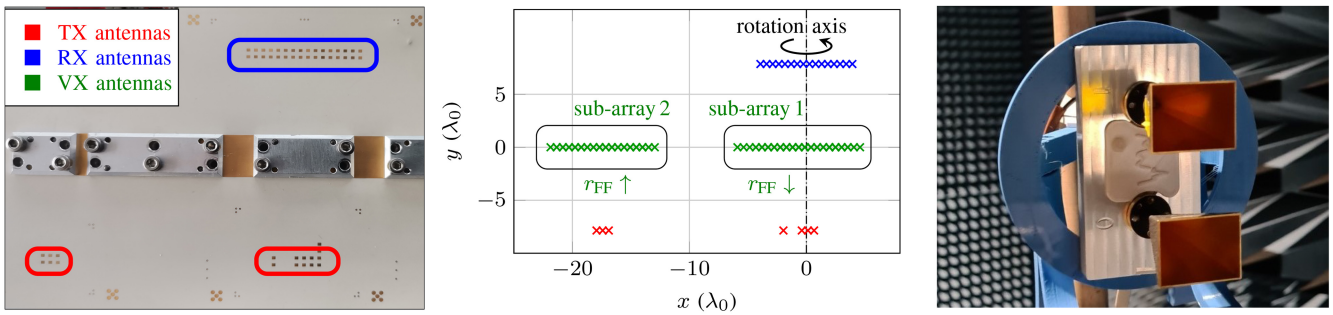

FIGURE 7. Hardware for calibration measurements with the multi active-target measurement setup. (a) Photograph of the array front-end for the investigation of occurring near-field effects and (b) the corresponding antenna positions. The virtual array is divided into two sub-arrays with lower and higher far-field distance r_{FF}. (c) ACT element for measurement setup with multiple ACTs.

TABLE 2. Overview of the radar parameters.

Ramp duration T	45.8 µs
Ramp repetition time T_{r}	440 µs
Center frequency f_c	78.5 GHz
RF bandwidth B	5 GHz
Number of chirps N_{c}	4096
Number of virtual channels $N_{\text{VX}} = N_{\text{TX}} \cdot N_{\text{RX}}$	$112 = 7 \cdot 16$
Virtual aperture size A_{V}	$26.4\,\lambda_0$

TABLE 3. Overview of the modulation frequencies of the three ACTs.

	f_{mod}	δR	δv
ACT 1	75.5 kHz	0.104 m	0.955 m/s
	151 kHz	0.207 m	1.906 m/s
ACT 2	32 kHz	0.044 m	0.347 m/s
	64 kHz	0.088 m	0.694 m/s
ACT 3	20 kHz	0.028 m	−0.868 m/s
	40 kHz	0.056 m	−1.736 m/s

A. HARDWARE DEMONSTRATOR

Fig. 7(d) shows the hardware setup for the following measurements. To analyse the effects occurring during the calibration process, especially when the far-field condition is violated, a tailored antenna array is employed. A photograph of the array is shown in Fig. 7. The antennas are fed by a FMCW radar system as described in [31], which is operated as listed in Tab. 2. Fig. 7(b) shows the antenna positions of the array. The resulting 1-D virtual array can be subdivided into 2 sub-arrays. Sub-array 1 has a lower far-field distance r_{FF} and sub-array 2 has a higher r_{FF}. Channels close to the rotation axis have the lowest r_{FF} as they can be assigned to a sub-array with reduced dimensions. By that, the near-field effects on calibration measurements violating the far-field condition can be directly compared to those measured in the far-field region.

B. SIGNAL SEPARATION IN CASE OF MULTIPLE ACTS

Fig. 7(c) shows an exemplary ACT of which three specimens are employed for the following experiments. To enable separation in the r-v domain, the ACTs operate at different modulation frequencies, listed in Tab. 3. In Fig. 8, the corresponding r-v plot of a radar measurement is depicted. All targets are ideally located at the same distance towards the rotation center of the positioning system.

For the determination of the phases of the ACTs, $2f_{\text{mod}}$ is additionally employed at each ACT [30]. It can be seen that in addition to the actual intended target responses, undesired targets appear from harmonics and intermodulation products.

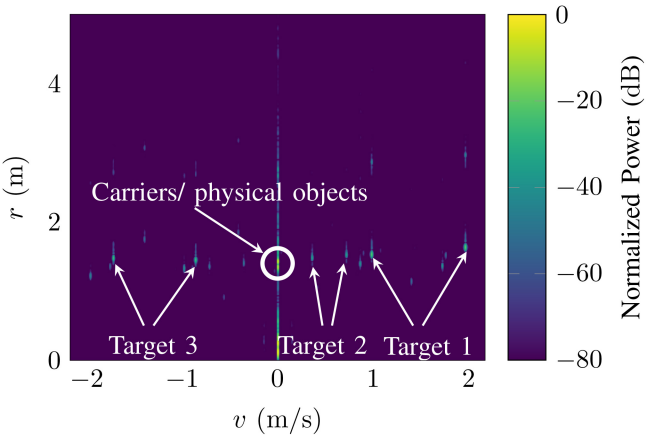

FIGURE 8. Resulting *r-v*-plot for the measurement setup. The modulation frequencies are listed in Tab. 3.

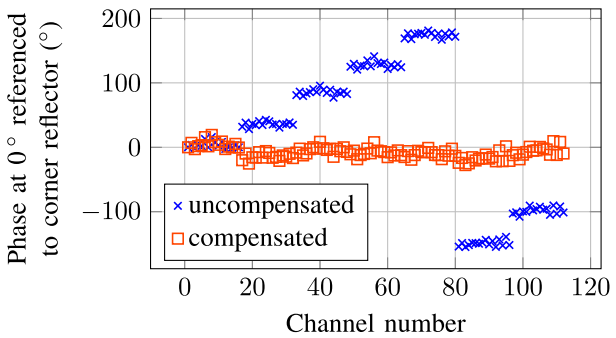

FIGURE 9. Measured phase at boresight direction. Asynchronous ACT phase leading to phase steps between the array transceivers.

Since the velocity cells in which the target appears can be set with high precision, the unwanted targets can be positioned in non-critical cells. This allows for undisturbed target extraction. By that, the extraction of the targets is quite convenient and windowing in the v domain can be used. In Fig. 8, the carriers are visible at $v = 0\,\mathrm{m/s}$.

C. COMPENSATION OF THE ACTIVE TARGET PHASE

As the phases of the active targets are not synchronized with the AUT, the phase relations between the channels are distorted, especially if time-domain multiplexing (TDM) is used. In the case of MIMO operation, these phase errors are not cancelled out by referring to a reference channel, as the ACT leads to different phase shifts on the array transceivers for each data point. This effect can be seen in Fig. 9 for the ACT placed at boresight direction. Since the time interval between active transmit periods is always the same, this leads to regular phase progressions along the transmitters. The compensation of this effect is described in detail in [30]. After the compensation, the phase shifts between the transceivers vanish.

D. CALIBRATION OF THE MEASUREMENT SETUP

In case of a passive calibration target, it is helpful to consider two Cartesian coordinate systems as depicted in Fig. 10. The

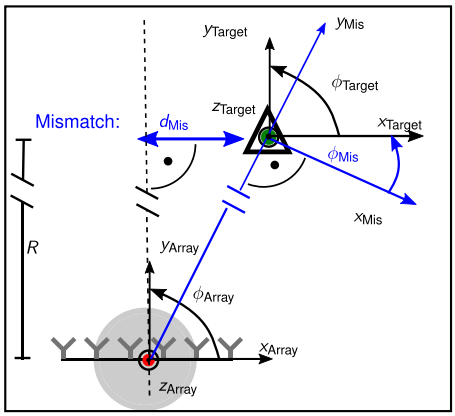

FIGURE 10. Geometric model of the calibration measurement setup using a single passive calibration target at distance R. Positioning mismatch of d_{Mis} translates into the target appearing at different target angle with the array as reference. This is described as a rotation of the target's coordinate system.

origin of the first coordinate system (AUT) is located at the rotation center, whereas the origin of the second system (Target) is located at the calibration target, which is considered as a point target. Ideally, the coordinate system origins only differ by a shift of the desired target distance. In practice, due to limited alignment accuracy, a misplacement along the x-axis, designated as d_{Mis}, is probable. This in turn results in an angular misalignment ϕ_{Mis}, and a rotation of the target's coordinate system as the y-axis of the target is defined to intersect with the arrays coordinate system's origin.

In the presence of N_{ACT} ACTs, $N_{\mathrm{ACT}}+1$ coordinate systems are needed to describe the measurement setup. To reduce this number of required systems to one, the ACTs are being related to one reference ACT. Thereby, all ACTs are combined into one coordinate system. In this work, this kind of alignment is understood as calibration of the measurement setup. In the following, a measurement setup of three ACTs, depicted in Fig. 11, is used.

1) DETERMINATION OF ACT PLACEMENTS

For the calibration of the measurement setup, ϕ_{Mis} has to be determined for $N_{\mathrm{ACT}}-1$ targets. Equally to the calibration with a passive calibration target, one active target and its corresponding coordinate system are employed as reference. The other targets are arranged in this reference coordinate system. The accuracy with which this reference target was positioned is decisive for the calibration quality. The procedure for arranging the targets in the reference coordinate system is referred to in this article as setup calibration.

Fig. 12 visualizes the calibration measurement scenarios for $\phi_{\mathrm{Array}} = \phi_{\mathrm{Target},n}$ with $n \in \{1, 2, 3\}$ as target identifier. If ideally positioned, the array response vector is the same for all depicted scenarios, as all targets appear in bore sight direction. The scanning angle is chosen to cover all angles ϕ_{Array}, where the targets are potentially placed, with some additional safety margin. As the measurement points recorded by Target 2 overlap with those of the other targets, it is deployed as reference target. The outermost target position is at $|\phi_{\mathrm{Array}}| = 20\,°$. Thus, the maximum scanning

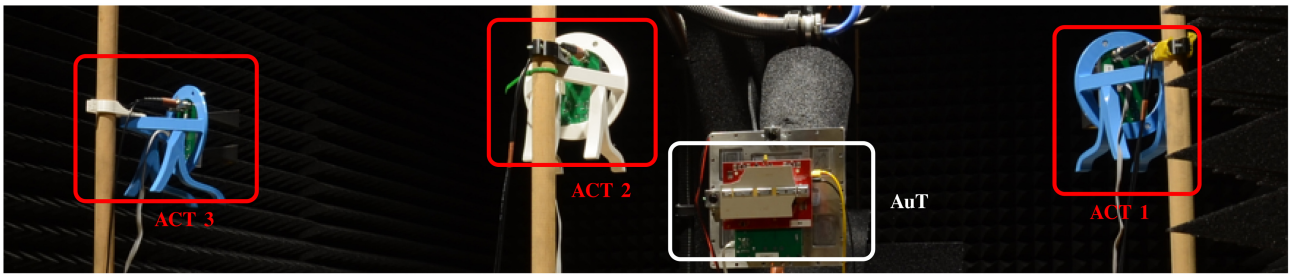

FIGURE 11. Calibration measurement setup using three ACTs. The ACTs are placed at $\phi_{\text{Target},1} = 20\,°$, $\phi_{\text{Target},2} = 0\,°$ and $\phi_{\text{Target},3} = -20\,°$ in the near-field of the AuT.

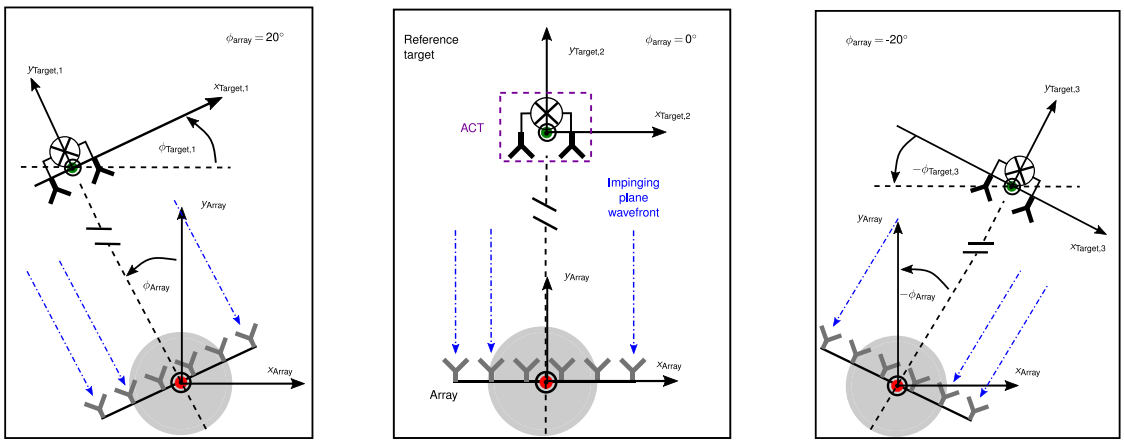

FIGURE 12. Visualization of the redundancy of data points for the rotation of the array over ϕ. Depicted are the scenarios (a) $\phi_{\text{Array}} = \phi_{\text{Target},1}$, (b) $\phi_{\text{Array}} = \phi_{\text{Target},2}$ and (c) $\phi_{\text{Array}} = \phi_{\text{Target},3}$ all ideally leading to identical steering vectors. ACTs are shown here for reason of clarity with only a mixer. The actual used ACTs consist of amplifiers as well.

angle is chosen as $\pm\,30\,°$ leading to a safety margin of $10\,°$. Therefore, the additional targets cover the intervals of $\boldsymbol{I}_1 = [-10\,°, 50\,°]$ and $\boldsymbol{I}_3 = [-50\,°, 10\,°]$, leading both to an overlay of $40\,°$ with the reference ACT.

For the alignment process of the targets, the array response vector a_2 at $\phi_{\text{Array}} = \phi_{\text{Target},2} = 0\,°$ is obtained by the reference target (2). To determine the angular position of the first target, the calibration matrix C_1 is obtained from the measured array response vectors over ϕ of Target 1. If Targets 1 and 2 are positioned ideally, the angle estimation performed with this calibration matrix C_1 and array response vector a_2 has its maximum at $\phi_{\text{Array}} = \phi_{\text{Target},1}$ as both result in the same array response vector, which can be seen in Figs. 12(a) and 12(b). To determine the angular position of the third target, an analogous procedure is performed with corresponding Figs. 12(b) and 12(c). The results of this DoA estimations for the angular position determinations are depicted in Fig. 13(a). The highest correlations appear at $20\,°$ and $-20\,°$, which are the desired target angles of Targets 1 and 3. Both targets were therefore positioned at the correct angles, relative to the reference Target 2. For possible misalignments, a correction value β_n can be obtained for the n-th ACT to take the offset into account.

For this procedure, near-field effects have no impact as the calibration matrix and the array phase responses are obtained in the same range cell. Furthermore, an uncalibrated array can be employed as the required calibration matrix is recorded from the non-reference targets during the calibration measurement of the setup. For the setup calibration shown here, the same array is deployed for the calibration of the measurement setup and later on as AUT. Alternatively, an array with greater aperture and higher angular resolution capabilities can be employed for the calibration of the measurement setup to enhance the accuracy. Overlapping regions reduce the efficiency of the multiple calibration target setup. They are only necessary during the setup calibration due to limited positioning accuracy of the ACTs. Afterwards, this overlap has to be avoided in order to obtain the greatest benefit from the calibration measurement setup. As general proof of concept, the mean phase deviations from the overlapping phase response vectors are depicted in Fig. 13(b), showing that the measurement results of different ACTs achieve approximately the same results. Therefore, the datasets obtained from the different targets can be combined with negligible phase deviations between the measurements.

2) DATA FUSION

After the alignment of calibration targets, the datasets C_n are combined for further processing to

$$C_{\text{Full}}^{I\times \text{N}_{\text{VX}}} = \begin{bmatrix} C_1 \\ \vdots \\ C_{N_{\text{ACT}}} \end{bmatrix} \widehat{=} \begin{bmatrix} C_1 \\ C_2 \\ C_3 \end{bmatrix}. \tag{10}$$

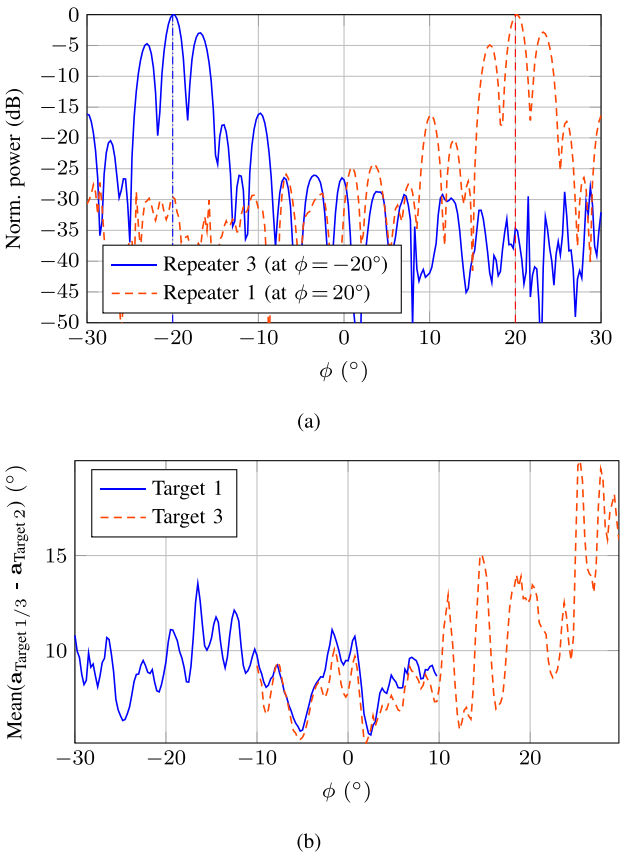

FIGURE 13. Evaluation of correct placement of the ACTs. (a) DoA estimation result with $\phi_{\text{Target},2} = 0°$ as array response vector $\boldsymbol{a}$ and the stored array response vectors of targets 1 and 3, respectively, as calibration matrix $\boldsymbol{C}$. (b) Mean deviation of array response vectors at the redundant angle areas with target 2 as reference.

The associated collection of related target angles is determined by

$$\Phi_{\text{Full}} = \begin{pmatrix} \Phi_1 + \beta_1 \\ \Phi_2 + \beta_2 \\ \vdots \\ \Phi_{N_{\text{ACT}}} + \beta_{N_{\text{ACT}}} \end{pmatrix} = \begin{pmatrix} \phi_1 + \beta_1 \\ \vdots \\ \phi_{\left\lceil \frac{I}{N_{\text{ACT}}} \right\rceil} + \beta_1 \\ \phi_{\left\lceil \frac{I}{N_{\text{ACT}}} \right\rceil + 1} + \beta_2 \\ \vdots \\ \phi_{\left\lceil \frac{2 \cdot I}{N_{\text{ACT}}} \right\rceil} + \beta_2 \\ \phi_{\left\lceil \frac{2 \cdot I}{N_{\text{ACT}}} \right\rceil + 1} + \beta_3 \\ \vdots \\ \phi_{\left\lceil \frac{N_{\text{ACT}} \cdot I}{N_{\text{ACT}}} \right\rceil} + \beta_{N_{\text{ACT}}} \end{pmatrix} \widehat{=} \begin{pmatrix} -30° + \beta_1 \\ \vdots \\ -10° + \beta_1 \\ -10° + \Delta\phi \ + \beta_2 \\ \vdots \\ 10° + \beta_2 \\ 10° + \Delta\phi \ + \beta_3 \\ \vdots \\ 30° + \beta_3 \end{pmatrix} \tag{11}$$

with β_n as correction value of the angular misplacement of the n-th ACT, determined during the calibration of the measurement setup. With the second ACT chosen as reference, $\beta_2 = 0$ follows.

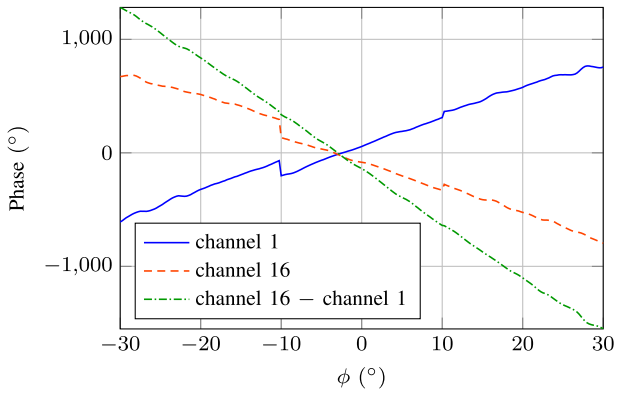

FIGURE 14. Obtained phase response after the fusion of the phase responses of the three different ACTs. The absolute phases of two channels and the difference are displayed.

As the targets are placed with finite accuracy, and the calibration of the measurement setup only includes an angular alignment, there may still be a range shift between targets. Fig. 14 shows the angle-dependent phase of two exemplary channels after fusion of the datasets. For those two channels, phase steps occur at $\phi_{\text{Array}} = 10°$. This is due to the existence of range deviations between the calibration targets. This range deviation is equal for all channels. Due to this fact, the steps can be eliminated by referencing the phase resulting in relative phases. During the calibration procedure, relative phases are calculated for further processing. In Fig. 14, based on the phase of channel 16 relative to channel 1, it can be seen that the steps have been compensated for. To summarize, range deviations lead to phase steps that cancel out when relative phase relations are calculated. Therefore, the calibration procedure employed here shows high robustness against small range deviations in the ACT placement.

IV. CALIBRATION WITH ACTIVE CALIBRATION TARGETS IN A NEAR-FIELD SETUP

To get the greatest benefit from the usage of N_{T} ACTs, they have to be placed with an angular spacing of

$$\Delta\phi = \frac{\phi_{\max} - \phi_{\min}}{N_{\text{T}}}. \tag{12}$$

By that, the overlapping of scanning regions covered by different ACTs is minimized.

For a calibration measurement setup using N_{T} ACTs, this condition can lead to sizes of the anechoic chamber that are undesirable. To reduce the requirements on the sizes of the chamber, the calibration employing multiple ACTs is performed in the near-field region of the antenna array.

A. MODELLING NEAR-FIELD EFFECTS

For the compensation of near-field effects, the path lengths have to be precisely known. In the following, a method based

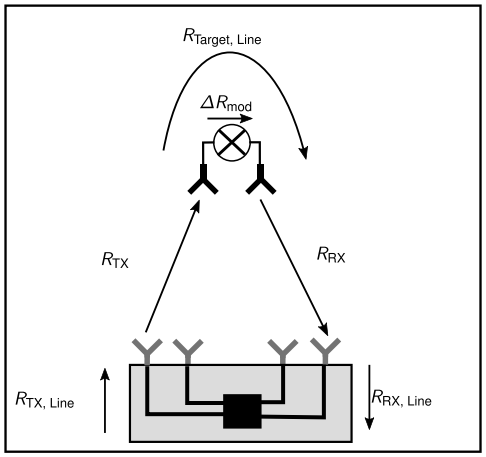

FIGURE 15. Model for the path propagation during the calibration measurement with an ACT.

on distance measurements employing the AUT is shown. The compensation of a calibration setup deploying a passive calibration target is described in detail in [19]. Thereby, the assumed antenna positions obtained from manufacturing data in combination with the target position are employed to model the spherical waves in order to compensate them.

In comparison to the calibration measurement setup with a passive calibration target, this setup with $N_{\text{T}} = 3$ increases the complexity. A propagation model of the setup is depicted in Fig. 15 for one ACT. The propagation path length measured of one exemplary channel adds up to

$$R = R_{\text{Frontend}} + R_{\text{FS}} + R_{\text{ACT}} \tag{13}$$

$$= R_{\text{TX, Line}} + R_{\text{RX, Line}} + R_{\text{TX}} + R_{\text{RX}} + R_{\text{ACT, Line}} + 2\Delta R_{\text{mod}} \tag{14}$$

with R_{Frontend} representing the paths along the transmission lines on the frontend consisting of the paths from the MMIC (monolithic microwave integrated circuit) to the TX antennas $R_{\text{TX, Line}}$ and the paths from the MMIC to the RX antennas $R_{\text{RX, Line}}$. R_{FS} models the paths propagated in free space and R_{ACT} considering the range shifts caused by the ACT. To model and to compensate the influence of spherical waves, R_{FS} has to be extracted from the measured distance R. Therefore, the other range shifts have to be determined and subtracted. According to (5), the modulation of the signal causes a shift in the measured range described by ΔR_{mod}. Therefore, the actual path length used to describe the propagation of the spherical wave is limited to R_{FS} and calculated with

$$R_{\text{FS}} = R_{\text{measured}} - (R_{\text{Frontend}} + R_{\text{ACT}}). \tag{15}$$

$$= R_{\text{measured}} - \big(R_{\text{TX, Line}} + R_{\text{RX, Line}} + R_{\text{ACT, Line}} + 2\Delta R_{\text{mod}}\big). \tag{16}$$

As the propagation speed through dielectric material differs from free space, the permittivity must be considered. Inserting (5) leads to [32]

$$R_{\text{FS}} = R_{\text{measured}} - \Big(\big(d_{\text{TX, Line}} + d_{\text{RX, Line}}\big)\sqrt{\varepsilon_{\text{r,Array}}} + d_{\text{ACT, Line}}\sqrt{\varepsilon_{\text{r,ACT}}} + \frac{f_{\text{mod}} T_c c}{B}\Big) \tag{17}$$

with $\sqrt{\varepsilon_{\text{r,Array}}}$ and $\sqrt{\varepsilon_{\text{r,ACT}}}$ describing the dielectric constants of the antenna array and the ACT, respectively. The physical lengths of the propagations paths on the AUT are defined as $d_{\text{TX, Line}}$, $d_{\text{RX, Line}}$ and $d_{\text{ACT, Line}}\sqrt{\varepsilon_{\text{r,ACT}}}$ for the ACT. To obtain the physical lengths of the AUT, manufacturing data is used. Simulations are deployed to gather the offsets $\Delta R_{\text{mod},i}$ caused by the modulation frequency f_{mod} for each ACT individually. Determining the distance propagated in free space enables the calculation of the correction steering vector $a_{\text{RX,corr}}$, which is employed for the compensation of the near-field influence [19]. Thereby, the target distance and roughly known positions from the antennas of the AUT are deployed to calculate the influences caused by spherical waves in order to compensate them from the data samples.

For the first channel as example, the evaluation of the calibration measurement shows a target distance of 1.52 m. The offset introduced by line lengths on the array is $R_{\text{TX, Line}} = 62\,\text{mm}$ and $R_{\text{RX, Line}} = 79\,\text{mm}$ leading to a total length of $R_{\text{Frontend}} = 141\,\text{mm}$. The range shift caused by the exemplary modulation frequency of 75.5 kHz can be read out from Tab. 3 as $\Delta R_{\text{mod}} = 104\,\text{mm}$. The offset introduced by line lengths on the ACT is $R_{\text{ACT, Line}} = 120\,\text{mm}$, which was obtained from scattering parameter measurement. The combination of all offsets is leading to a target distance of

$$R_{\text{Target}} = 1.52\,\text{m} - \big(\Delta R_{R_{\text{Array}}} + \Delta R_{\text{mod}} + \Delta R_{\text{Target, Line}}\big) = 1.52\,\text{m} - 0.365\,\text{m} = 1.155\,\text{m}. \tag{18}$$

This is the target distance needed for the compensation of near-field effects.

By means of simulation the phase changes introduced by the near-field are calculated to subtract them from the measured phase responses [19]. After this compensation, the spherical wave influences are compensated for.

B. MEASUREMENT RESULTS

The results with and without the near-field compensation are compared in Fig. 16. As reference within the antenna array, the channels of sub-array 1 (see Fig. 7(b)) are included in the first two subfigures and due to their lower far-field condition here referenced as FF channels. For evaluation, a reference calibration is performed in the far-field of the antenna array with a corner reflector as calibration target. Figs. 16(a) and 16(b) show the deviation of the determined calibration parameters from the near-field with and without the compensation compared to the calibration parameters determined by the reference calibration. Fig. 16(a) shows the effect on the determined VX positions. The compensation causes a higher deviation for 3 of 48 channels with a strong

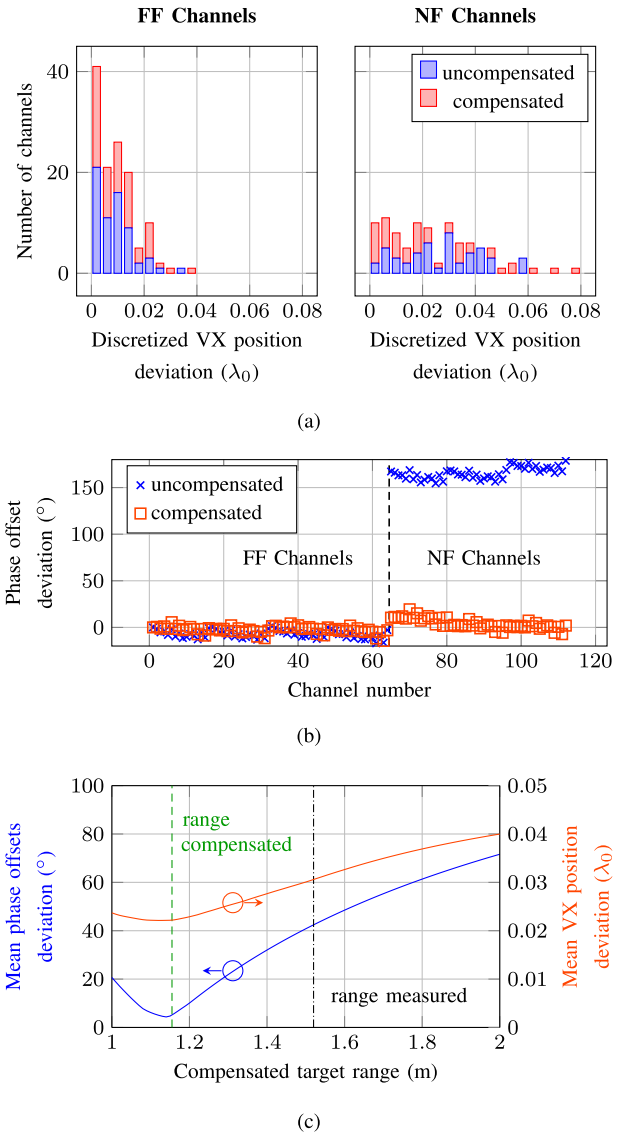

FIGURE 16. Derived calibration parameters from near-field calibration measurement. (a) Comparison of determined antenna phase centers with and without compensation of near-field effects. (b) Comparison of obtained phase offsets with and without compensation of near-field effects. (c) Mean phase offsets deviation of near-field channels for different target distances chosen for compensation.

violation of the far-field condition. The mean deviation of the NF channels decreases from 0.056 λ_0 to 0.022 λ_0 when the compensation is applied. In Fig. 16(b), the effect of the compensation on the phase offsets is shown. If uncompensated, the phase offsets differ considerably. The near-field compensation decreases the mean deviation of NF channels from 164.2° to 5.2°, thus showing a significant impact. The mean deviation over all channels amounts to 4.1° for the phase offsets and 0.014 λ_0 for the VX positions. In case of an erroneous target distance on the spherical wave model, the compensation quality suffers. If the distance is too large, the spherical wave influences are insufficiently compensated. In the case of an underestimated target distance, larger near-field influences are modeled, overcompensating the actual ones. This dependency on the correct target distance is depicted in Fig. 16(c). If the measured target distance is chosen without taking the different offsets into account, the mean deviation of the VX positions increases for the NF channels from 0.022 λ_0 to 0.031 λ_0 and the phase offsets from 5.2° to 42.3°. In case of the phase offsets the mean deviation of NF channels increases by 715 %. It should be noted that the lowest mean phase offsets deviation is reached for a compensation distance of 1.141 m leading to 4.3°. The difference of 14 mm can be caused by tolerances of the permittivities used for range offset calculation, line lengths, inaccuracies during the positioning of the measurement set up or noise influences on the phase responses. Although the compensation distance of the lowest mean is not hit, the result is close to the optimum.

V. CONCLUSION

In this article, a measurement setup for phased array calibration, based on the application of ACTs, is proposed. With this setup, it is possible to reduce the calibration measurement effort significantly without a reduction of data points recorded, ensuring high quality array calibrations. This is done by recording multiple data points in parallel. It is shown that systematic errors from the active target architecture can be compensated by a simulation model and an initial calibration of the measurement setup. To reduce the requirements on the anechoic chamber sizes, the calibration with three ACTs was performed in the near-field region of the AUT. Furthermore, the calibration features high robustness against small range offsets of the ACTs. Moreover, ACTs make the calibration measurement much more flexible, as the choice of the ACT antennas influences the angular beamwidth and the coverage of the calibration target. The selection of amplifiers leads to an easily adaptable signal strength. By taking all the relevant effects into account, the quality of a calibration measurement performed in the far-field region of the AUT can be restored. Subsequently, the proposed setup enables a significant acceleration of angular array calibrations with relaxed requirements with respect to the measurement area without degrading the calibration quality.

REFERENCES

[1] C. Waldschmidt, J. Hasch, and W. Menzel, "Automotive radar—From first efforts to future systems," *IEEE J. Microw.*, vol. 1, no. 1, pp. 135–148, Jan. 2021.
[2] M. Nosrati, S. Shahsavari, S. Lee, H. Wang, and N. Tavassolian, "A concurrent dual-beam phased-array doppler radar using MIMO beamforming techniques for short-range vital-signs monitoring," *IEEE Trans. Antennas Propag.*, vol. 67, no. 4, pp. 2390–2404, Apr. 2019.
[3] T. Kraus, G. Krieger, M. Bachmann, and A. Moreira, "Spaceborne demonstration of distributed SAR imaging with TerraSAR-X and TanDEM-X," *IEEE Geosci. Remote Sens. Lett.*, vol. 16, no. 11, pp. 1731–1735, Nov. 2019.
[4] P. Hügler, F. Roos, M. Schartel, M. Geiger, and C. Waldschmidt, "Radar taking off: New capabilities for UAVs," *IEEE Microw. Mag.*, vol. 19, no. 7, pp. 43–53, Nov./Dec. 2018.
[5] W. Menzel, "Millimeter-wave radar for civil applications," in *Proc. 7th Eur. Radar Conf.*, Sep. 2010, pp. 89–92.

[6] S. S. Ahmed, A. Genghammer, A. Schiessl, and L.-P. Schmidt, "Fully electronic *E*-band personnel imager of 2 m^2 aperture based on a multistatic architecture," *IEEE Trans. Microw. Theory Techn.*, vol. 61, no. 1, pp. 651–657, Jan. 2013.

[7] A. Di Serio, P. Hügler, F. Roos, and C. Waldschmidt, "2-D MIMO radar: A method for array performance assessment and design of a planar antenna array," *IEEE Trans. Antennas Propag.*, vol. 68, no. 6, pp. 4604–4616, Jun. 2020.

[8] J. Wittemeier, A. M. Ahmed, T. N. Tran, A. Sezgin, and N. Pohl, "3D localization using a scalable FMCW MIMO radar design," in *Proc. German Microw. Conf. (GeMiC)*, 2020, pp. 100–103.

[9] D. Schwarz, N. Riese, I. Dorsch, and C. Waldschmidt, "System performance of a 79 GHz high-resolution 4D imaging MIMO radar with 1728 virtual channels," *IEEE J. Microw.*, vol. 2, no. 4, pp. 637–647, Oct. 2022.

[10] A. Dürr et al., "On the calibration of mm-Wave MIMO radars using sparse antenna arrays for DoA estimation," in *Proc. 16th Eur. Radar Conf. (EuRAD)*, Oct. 2019, pp. 349–352.

[11] B. Friedlander and A. Weiss, "Direction finding in the presence of mutual coupling," *IEEE Trans. Antennas Propag.*, vol. 39, no. 3, pp. 273–284, Mar. 1991.

[12] A. J. Weiss and B. Friedlander, "Mutual coupling effects on phase-only direction finding," *IEEE Trans. Antennas Propag.*, vol. 40, no. 5, pp. 535–541, May 1992.

[13] I. Gupta, J. Baxter, S. Ellingson, H.-G. Park, H. S. Oh, and M. G. Kyeong, "An experimental study of antenna array calibration," *IEEE Trans. Antennas Propag.*, vol. 51, no. 3, pp. 664–667, Mar. 2003.

[14] C. Vasanelli et al., "Calibration and direction-of-arrival estimation of millimeter-wave radars: A practical introduction," *IEEE Antennas Propag. Mag.*, vol. 62, no. 6, pp. 34–45, Dec. 2020.

[15] M. Lanne, A. Lundgren, and M. Viberg, "Calibrating an array with scan dependent errors using a sparse grid," in *Proc. 40th Asilomar Conf. Signals, Syst. Comput.*, 2006, pp. 2242–2246.

[16] A. Dürr, M. Linder, D. Schwarz, T. Frey, and C. Waldschmidt, "Efficient calibration of very large mm-Wave radars by virtual phase center analysis," in *Proc. 18th Eur. Radar Conf. (EuRAD)*, 2022, pp. 521–524.

[17] A. Dürr, M. Linder, D. Schwarz, and C. Waldschmidt, "Highly efficient angular array calibration based on the modal wave expansion technique," *IEEE Open J. Antennas Propag.*, vol. 2, pp. 938–948, 2021.

[18] J. Geiss, E. Sippel, and M. Vossiek, "A practical concept for precise calibration of MIMO radar systems," in *Proc. 18th Eur. Radar Conf. (EuRAD)*, 2022, pp. 405–408.

[19] A. Dürr, B. Schneele, D. Schwarz, and C. Waldschmidt, "Range-angle coupling and near-field effects of very large arrays in mm-Wave imaging radars," *IEEE Trans. Microw. Theory Techn.*, vol. 69, no. 1, pp. 262–270, Jan. 2021.

[20] G. Körner, D. Oppelt, J. Adametz, and M. Vossiek, "Novel passive calibration method for fully polarimetric near field MIMO imaging radars," in *Proc. 12th German Microw. Conf. (GeMiC)*, 2019, pp. 150–153.

[21] H. Krim and M. Viberg, "Two decades of array signal processing research: The parametric approach," *IEEE Signal Process. Mag.*, vol. 13, no. 4, pp. 67–94, Jul. 1996.

[22] J. Li and P. Stoica, *MIMO Radar Signal Processing*. Hoboken, NJ, USA: Wiley, 2009.

[23] T. E. Tuncer and B. Friedlander, *Classical and Modern Direction-of-Arrival Estimation*. Amsterdam, The Netherlands: Academic, 2009.

[24] A. Dürr, M. Linder, and C. Waldschmidt, "Increasing the efficiency and robustness of angular radar calibration by exploiting phase symmetry," in *Proc. 17th Eur. Radar Conf. (EuRAD)*, Jan. 2021, pp. 30–33.

[25] P. Schoeder, B. Schweizer, A. Grathwohl, and C. Waldschmidt, "Multitarget simulator for automotive radar sensors with unknown chirp-sequence modulation," *IEEE Microw. Wireless Compon. Lett.*, vol. 31, no. 9, pp. 1086–1089, Sep. 2021.

[26] J. Iberle, M. A. Mutschler, P. A. Scharf, and T. Walter, "A radar target simulator concept for close-range targets with micro-doppler signatures," in *Proc. 12th German Microw. Conf. (GeMiC)*, 2019, pp. 198–201.

[27] P. Schoeder, V. Janoudi, B. Meinecke, D. Werbunat, and C. Waldschmidt, "Flexible direction-of-arrival simulation for automotive radar target simulators," *IEEE J. Microw.*, vol. 1, no. 4, pp. 930–940, Oct. 2021.

[28] B. Meinecke, M. Steiner, J. Schlichenmaier, J. Hasch, and C. Waldschmidt, "Coherent multistatic MIMO radar networks based on repeater tags," *IEEE Trans. Microw. Theory Techn.*, vol. 67, no. 9, pp. 3908–3916, Sep. 2019.

[29] V. Winkler, "Range doppler detection for automotive FMCW radars," in *Proc. Eur. Microw. Conf.*, 2007, pp. 1445–1448.

[30] D. Werbunat, B. Meinecke, M. Steiner, and C. Waldschmidt, "Phase recovery in sensor networks based on incoherent repeater elements," in *IEEE/MTT-S Int. Microw. Symp. Tech. Dig.*, 2020, pp. 1149–1152.

[31] B. P. Ginsburg et al., "A multimode 76-to-81GHz automotive radar transceiver with autonomous monitoring," in *Proc. IEEE Int. Solid-State Circuits Conf. (ISSCC)*, 2018, pp. 158–160.

[32] D. Pozar, *Microwave Engineering*, 4th ed. Hoboken, NJ, USA: Wiley, 2012.

MATTHIAS LINDER (Graduate Student Member, IEEE) received the M.Sc. degree from Ulm University, Ulm, Germany, in 2020, where he is currently pursuing the Ph.D. degree.

From 2018 to 2019, he was an Intern with HUBER+SUHNER, Herisau, Switzerland. In 2020, he joined the Institute of Microwave Engineering, Ulm University. His current research interests focus on the calibration of electrical large antenna arrays with significantly reduced requirements in space and effort.

BENEDIKT MEINECKE (Member, IEEE) received the M.Sc. degree in electrical engineering with a focus on communication technology from Ulm University, Ulm, Germany, in 2017, where he is currently pursuing the Ph.D. degree in electrical engineering with the Institute of Microwave Engineering. His research interests include system concepts for multistatic coherent radar networks and the accompanying signal processing.

ENES HALICI received the M.Sc. degree in electrical engineering (with a focus on Hardware System Engineering) from the University of Ulm, Ulm, Germany, in 2022. In 2022, he joined Tesat-Spacecom GmbH & Co. KG, Backnang, Germany, where he is currently working on RF components for telecommunication satellites.

DOMINIK SCHWARZ (Graduate Student Member, IEEE) received the M.Sc. degree from Ulm University, Ulm, Germany, in 2018, where he is currently pursuing the Ph.D. degree.

From 2011 to 2018, he was a Student Trainee with Hensoldt Sensors, Ulm. In 2018, he joined the Institute of Microwave Engineering, Ulm University. His current research interest includes automotive MIMO radars with a focus on high bandwidths, high channel counts, 2-D-DoA estimation, and novel multilayer PCB structures at millimeter-wave frequencies.

Mr. Schwarz was a recipient of the Ingenieure für Kommunikation Award in 2016 and the Argus Science Award in 2019.

CHRISTIAN WALDSCHMIDT (Fellow, IEEE) received the Dipl.-Ing. (M.S.E.E.) and the Dr.-Ing. (Ph.D.E.E.) degrees from the University Karlsruhe (TH), Karlsruhe, Germany, in 2001 and 2004, respectively.

From 2001 to 2004, he was a Research Assistant with the Institut für Höchstfrequenztechnik and Elektronik, TH, Germany. Since 2004, he has been with Robert Bosch GmbH, in the business units Corporate Research and Chassis Systems. He was heading different research and development teams in microwave engineering, RF-sensing, and automotive radar. In 2013, he returned to academia. He was appointed as the Director of the Institute of Microwave Engineering, University of Ulm, Germany, as a Full Professor. He authored or coauthored over 200 scientific publications and more than 20 patents. His research topics focus on radar and RF-sensing, mm-wave and submillimeter-wave engineering, antennas and antenna arrays, RF, and array signal processing.

Dr. Waldschmidt is a reviewer for multiple IEEE Transactions and many IEEE conferences in the field of microwaves. He has been a co-recipient of 12 best paper awards since 2014. He is the Chair of the IEEE MTT-29 Technical Committee on Microwave Aerospace Systems and served as the Chair of MTT-27 Technical Committee on Wireless Enabled Automotive and Vehicular Applications. He was the two-time TPC Chair and the General Chair of the IEEE MTT International Conference on Microwaves for Intelligent Mobility. Since 2018, he has been serving as an Associate Editor for IEEE MICROWAVE WIRELESS COMPONENTS LETTERS. He is a member of the Executive Committee Board of the German MTT/AP Joint Chapter and a Member of the German Information Technology Society.